Design and Characterization of Next-Generation Micromirrors Fabricated in a Four-Level, Planarized Surface-Micromachined Polycrystalline Silicon Process

M. Adrian Michalicek	John H. Comtois	Carole Craig Barron
USAF Phillips Laboratory	USAF Phillips Laboratory	Sandia National Laboratories
Space Technologies Directorate	Space Technologies Directorate	Dept. 1325 / MS 1080
3550 Aberdeen Avenue SE	3550 Aberdeen Avenue SE	P. O. Box 5800
Kirtland AFB, NM 87117-5776	Kirtland AFB, NM 87117-5776	Albuquerque, NM 87185
Voice: (505) 846-4955	Voice: (505) 846-5813	Voice: (505) 844-6583
Fax: (505) 846-5815	Fax: (505) 846-5815	Fax: (505) 844-2991
michalia@plk.af.mil	comtoisj@plk.af.mil	barroncc@smtplink.mdl.sandia.gov

ABSTRACT

This paper describes the design and characterization of several types of micromirror devices to include process capabilities, device modeling, and test data resulting in deflection versus applied potential curves. These micromirror devices are the first to be fabricated in the state-of-the-art four-level planarized polysilicon process available at Sandia National Laboratories known as the Sandia Ultra-planar Multi-level MEMS Technology (SUMMiT). This enabling process permits the development of micromirror devices with near-ideal characteristics which have previously been unrealizable in standard three-layer polysilicon processes. This paper describes such characteristics as elevated address electrodes, individual address wiring beneath the device, planarized mirror surfaces using Chemical Mechanical Polishing (CMP), unique post-process metallization, and the best active surface area to date.

This paper presents the design, fabrication, modeling, and characterization of several variations of Flexure-Beam (FBMD) and Axial-Rotation Micromirror Devices (ARMD). The released devices are first metallized using a standard sputtering technique relying on metallization guards and masks that are fabricated next to the devices. Such guards are shown to enable the sharing of bond pads between numerous arrays of micromirrors in order to maximize the number of on-chip test arrays. The devices are modeled and then empirically characterized using a laser interferometer setup located at the Air Force Institute of Technology (AFIT) at Wright-Patterson AFB in Dayton, Ohio. Unique design considerations for these micromirror devices and the SUMMiT process are also discussed. The models are then compared with the empirical data to produce a complete characterization of the devices in a deflection versus applied potential curve.

INTRODUCTION

Micromirror devices have become some of the most recognized and useful spatial light modulators (SLM) and have been successfully implemented in recent years in a variety of military and commercial systems. The designers of these devices, however, have been faced with a number of engineering compromises which typically limit the desired or ideal operation. For instance, many forms of micromirrors fabricated in the standard three-layer polysilicon process known as Multi-User MEMS Process (MUMPS) have been designed with reduced reflective surface area in order to make room for the flexures which support the mirror or were scarred with serious topographical effects in the reflective surface due to

DISCLAIMER

features fabricated beneath it. Both of these drawbacks were previously unavoidable in most, if not all, commercially available fabrication services.

Ideally, an advanced fabrication process would remove these and other drawbacks so that a more functional micromirror device can be realized. The devices studied in this paper were fabricated in such a process. Ultimately, the designer is able to develop micromirrors with dense wiring beneath the device for large arrays, raised address electrodes, thin flexures for reduced address potentials, and planarized mirror surfaces with only 1 μm design rules which makes possible optical efficiencies of 98% or better. Added to this, several design techniques such as metallization shielding, shorting, and trapped oxide wiring can be employed to further enable the designer to optimize micromirror devices.

FABRICATION

The micromirrors presented in this paper were fabricated in the Sandia Ultra-planar Multi-level MEMS Technology (SUMMiT) process commercially available through the Sandia Agile MEMS Prototyping, Layout tools, and Education (SAMPLE) service [1]. As in other surface-micromachining processes, micromechanical devices are formed in SUMMiT by the alternate deposition of structural polysilicon layers and sacrificial oxide layers. The polysilicon layers are patterned (using the same advanced photolithography technology employed by the microelectronics industry) to form intricate structures such as motors, gears, mirrors, and various sensors. Cuts made through the oxide layers are used to anchor the upper structural levels to the silicon substrate or underlying structures. At the end of the process the sacrificial layers, as the name suggests, are removed using a hydrofluoric acid release etch which frees the device to move relative to the substrate.

Although manufacturing processes similar to SUMMiT have existed for years, this process represents a major leap forward for the MEMS technology field in several respects. First, the complexity of the micromachines which can be manufactured in a given process is a function of the number of independent layers of structural material the technology provides. A single independent level of structural material limits designers to simple sensors whereas geared mechanisms require two independent levels (one to form the hubs and the other the moving gears) and motorized geared mechanisms require a minimum of three independent levels. The SUMMiT process is the only commercial MEMS process in the world to offer three releasable structural layers (Poly-1 through Poly-3) above the ground layer (Poly-0).

Additionally, the SUMMiT process offers other unique advantages which include planarization of the upper polysilicon layer, ultra-low-stress structural material, design rules and feature sizes of only 1 μm with 0.1 μm mask resolution, and the ability to make flanged gear hubs. The planarization eliminates any unwanted mirror surface topography which is normally induced by the conformal deposition of one layer over the mechanical features of the underlying layers. The uppermost sacrificial oxide is planarized using Chemical Mechanical Polishing (CMP) so that the following structural layer is flat [1]. For instance, a 100 μm mirror showed only 17 nm of curvature across the device. Furthermore, the deposition of ultra-low-stress polysilicon developed by Sandia enables SUMMiT designers to use larger expanses of structural material without concern that the device will curl due to internal stress.

Much of the current micromirror research conducted using the SUMMiT process is a continuation of similar work begun using the Multi-User MEMS Process (MUMPS) which is commercially available through the Microelectronics Center of North Carolina (MCNC) [2]. This process has been widely used in most university, commercial, and military applications involving simple micromechanical structures. Unfortunately, the designer may soon realize that a more complex process is needed to fully optimize many types of micromirror devices.

Ultimately, the SUMMiT process was not used to replace the MUMPS process, but rather to be employed only after the limits in design and operation of micromirror devices had been reached without satisfying the necessary requirements. Only after significant micromirror design experience using the MUMPS process was enough technical understanding acquired to sufficiently exploit the SUMMiT process for next-generation devices.

For instance, the Flexure-Beam device shown in Figure 1(a) was part of micromirror research conducted at the Air Force Institute of Technology (AFIT) which involved numerous versions and generations of devices fabricated in the MUMPS process [3].
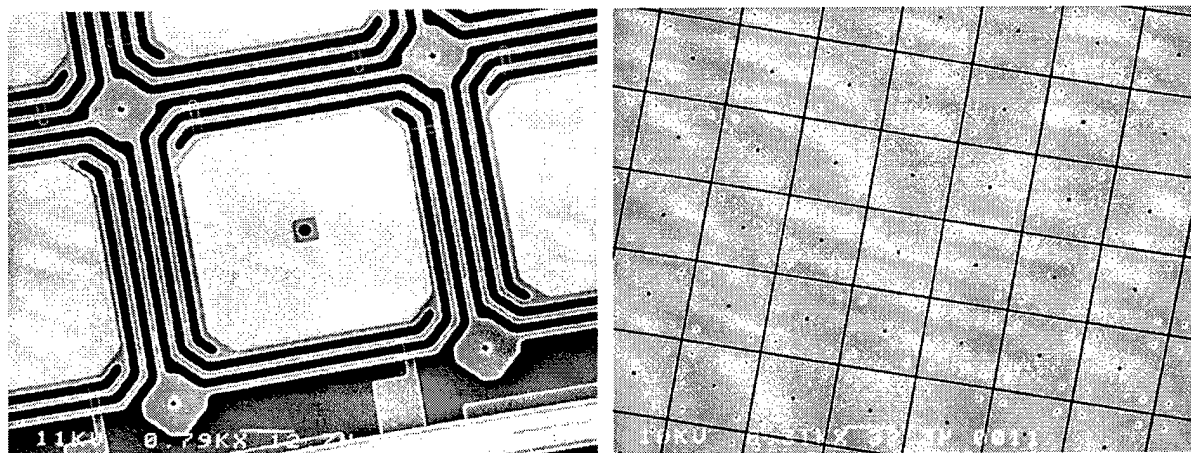
(a) Devices fabricated in MUMPS process [3]   (b) Devices fabricated in SUMMiT process

Figure 1. Micrographs of two generations of Flexure-Beam Micromirror Device arrays.

This device was successfully used to test both ideal and advanced micromirror models and provided much of the information needed to adequately design micromirrors specifically for the SUMMiT process. As a direct result of the SUMMiT features, micromirror devices, such as those in the array shown in Figure 1(b), can be made with significantly greater optical efficiencies and lower address potentials than similar devices fabricated in other processes.
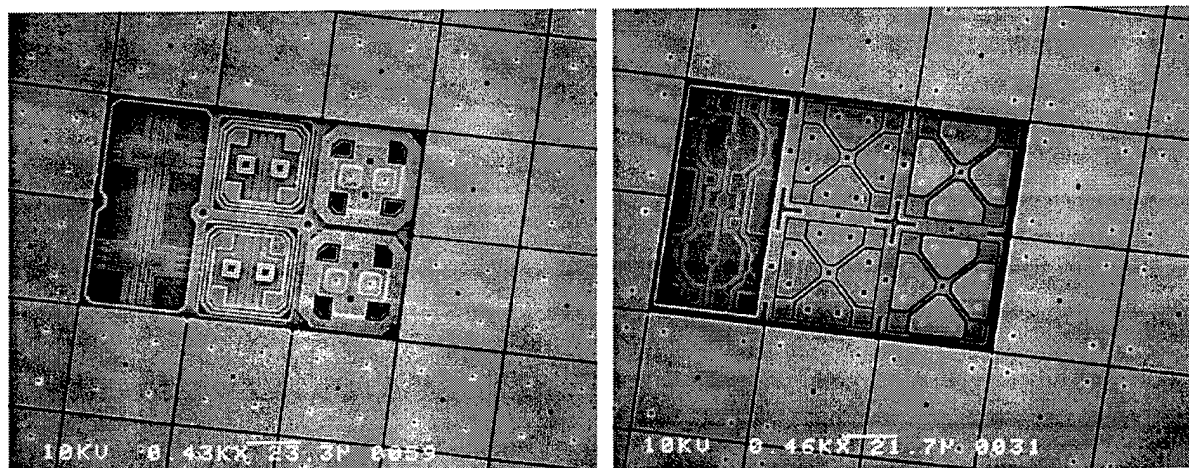
DESIGN

Given the capabilities of the SUMMiT process, the design goal for the first-generation of micromirrors was simply to create a variety of Flexure-Beam and Axial-Rotation devices which exploit these capabilities and thereby demonstrate improved performances over current devices. This process is simply ideal for micromirror fabrication and some of the devices created were enabled by its unique features.

The first and most valuable design characteristic of these devices is the upper layer of planarized polysilicon which is used as the mirror surface. Since it is the third releasable layer, the flexures and address electrodes can easily be placed under the surface of the device. The planarization of the mirror surface eliminates the standard design trade-off between placing flexures beneath the mirror, which would induce severe topographical effects in the surface, and placing the flexures around the edge of the mirror, which dramatically reduces the active area of an array of devices. Using the SUMMiT process, the support features of micromirror devices can be hidden in order to maximize optical efficiency while completely eliminating adverse topographical effects in the mirror surface.

Another design characteristic is the use of the additional layer of polysilicon provided in the fabrication process. With three releasable layers of varying thickness available to the

engineer, micromirror devices can become more complex and be easily designed to behave as desired. For instance, the Flexure-Beam device shown in Figure 2(a) illustrates the use of these layers in order of fabrication. First, the Poly-0 wiring, which runs beneath the device, allows for large arrays of individually addressable devices. The Poly-0 landing pads shown between the wires are connected to the address electrode via support posts and are simply shorted to the address wire of choice. The compliant flexures are made in Poly-1 which is the thinnest (only 1 µm thick) of the structural layers in order to reduce the spring constant and therefore the address potential. To further reduce the potential, the address electrode is elevated using the Poly-2 layer so that only a 2 µm resting separation of the address plates is realized. The planarized Poly-3 mirror surface is then anchored to the flexures through holes cut in the address electrode. As a result of exploiting each layer in this design process, this device can be actuated at an address potential directly compatible with CMOS electronics.

(a) Flexure-Beam Micromirror Device   (b) Axial-Rotation Micromirror Device

Figure 2. Design depiction by process layers for two types of micromirror devices.

The Axial-Rotation device shown in Figure 2(b) also uses the same wiring and thin flexure design, but has four distinct address electrodes which are constructed from stacked Poly-1 and Poly-2 layers. Due to the short flexures, it was known that this device would require a large address potential and it became desirable to stiffen the electrodes to prevent them from bending upward toward the mirror. The Poly-0 wiring is a repeated pattern shared with each device so that the entire array can be aimed at a desired angle based on the relative address potential applied to the four address electrodes.

At present, the SUMMiT fabrication process does not offer the deposition of a metal layer which is often used as the reflective material on micromirror devices. However, since many applications of such devices require a sensitivity to specific wavelengths, it would be useful to deposit a material of choice which is selected for its reflective properties. Therefore, these micromirrors were fabricated with a metallization shield surrounding each device and also the entire array, which will allow for post-process metallization after the devices are released. These shields prevent shorting address wires which run beneath and around the micromirrors. An advantage of this technique is that there are no design rules to limit the amount of reflective surface on the mirror. For instance, some processes require a 2 µm margin of underlying polysilicon around a metallized area which drastically reduces the active area of the mirror. The post process metallization covers 100% of the exposed mirror surface.

METALLIZATION

The shields surrounding the arrays are 350 µm wide which allows for a very rough positioning of a masking surface surrounding the array of choice and protecting the bond pads and other wiring. The address wiring runs beneath this shield which is secured with anchors and trapped oxide in order to provide more structural support when masking off the micromirror arrays. Figure 3 illustrates the masking and metallization of one FBMD test chip and two ARMD test chips. Small strips cut from ESD protection pouches, used as the masking material, were placed around the edges of the arrays using double-sided tape affixed to a flat work surface. This task was easily completed by hand under a microscope. The larger white mask shown in Figure 3(a) was used only to help identify the chips in the illustration. These test chips were metallized with 150 nm of gold as shown in Figure 3(b).
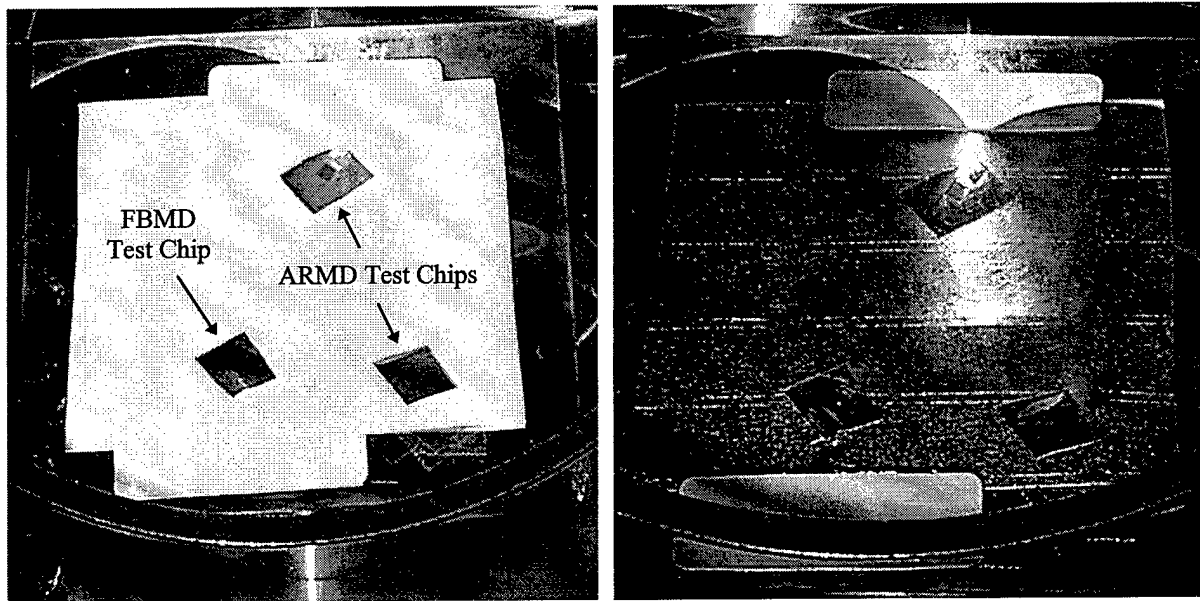

| (a) After masking off selected arrays | (b) After 150 nm gold deposition |

Figure 3. Photographs illustrating post-process metallization of micromirror device arrays.

This post-process metallization procedure can be used to deposit a desired material and thickness on various micromirror arrays which makes it adequate for testing purposes and most applications. However, depending on the type of sputtering machine used, it may not be an ideal line-of-sight deposition. This test demonstrated signs of significant undercutting of the masking material up to a worst-case of approximately 45 degrees. Therefore, either extreme care must be taken when placing masks around the array or a precision sputtering machine must be used to ensure that no wiring or bond pads are shorted during the process.

A new post-process metallization approach has been developed which is currently in fabrication on second-generation test chips. This technique builds the metallization shield into the design layout so that no post-process masking is needed. This shield isolates each bond pad and allows no address wiring to be exposed anywhere on the chip. The support posts of this shield are recessed at least a distance equal to the height of the shield so that even the worst-case metallization will not short the bond pads to the shield. It is beneficial to use this shield as the ground plane, so a significant margin around the bond pads must be maintained to prevent shorting during bonding and packaging of the chips.

Post-process metallization can also be used to extend the functionality of test chips containing several large arrays of individually addressable micromirrors where the number of devices drastically outnumbers the bond pads that can be placed around the edge of the test chip. A window in the metallization shield can be placed directly over a gap in the address wiring which connects all of the arrays of test devices. The micromirror devices requiring the largest address potential are wired directly to the bond pads and subsequent arrays of devices can be shorted to active address wires by the metallization process in order of decreasing address potential or by testing preference. Figure 4(a) shows how such wiring interconnects are used between two Flexure-Beam micromirror arrays. When the second array is masked and metallized, the wiring gaps are shorted, thereby connecting its devices to the bond pads.
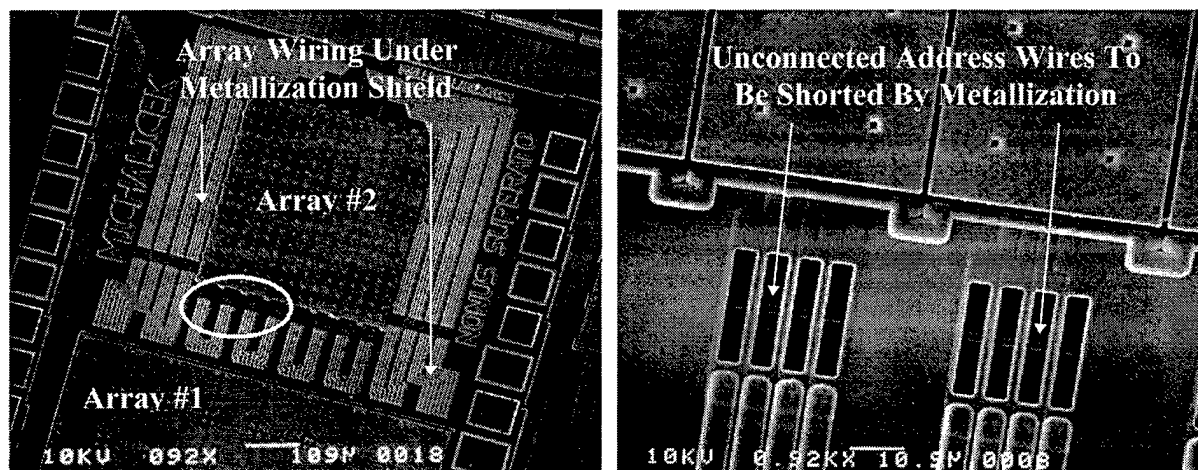
(a) Wide view of contacts between arrays   (b) Magnified view of circled region

Figure 4. Micrographs of micromirror array interconnects used to share bond pad wiring.

The probe pads that are visible in this micrograph were shorted with the address wiring in order to allow for direct testing of specific micromirror devices within each of the arrays. The magnified view in Figure 4(b) illustrates the gap in the address wiring which is visible beneath the metallization shield. Using this process, it was shown that a deposition of approximately 150 nm of gold resulted in sufficient electrical contacts between devices in the second micromirror array and the bond pads. Again, care must be taken during the metallization process to prevent shorting between address lines due to undercutting the shield. Ultimately, this technique easily allowed for testing of five arrays of at least 64 individually addressable micromirrors by the sharing of bond pads surrounding the arrays.

MODELING

The modeling of these micromirror devices is accomplished by simply balancing the electrostatic force of a parallel plate capacitor with the restoring spring forces supplied by the support flexures of the device [3]. These flexures are easily modeled using standard beam theory given the material properties and dimensions of the structural layers used in the fabrication process. For most micromirror devices and applications, an ideal model of the characteristic behavior can be used. Such a model, however, does not include effects of electrostatic fringing, thermal variances, frequency dependence, mirror surface deformations, or cross-talk from adjacent devices. As the address electrode area of a given device decreases, the fringing effects become more significant and more voltage is required to achieve a desired

displacement. As the size of the device increases, however, the mirror surface tends to sag and deform during actuation. The other characteristics addressed by advanced models can be neglected if the proper operating conditions are selected for testing [4].

It should be noted that various characteristics of new micromirror designs may not have previously been addressed by even the most advanced device models. For instance, the elevated address electrode on the Flexure-Beam device shown in Figure 2(a) will exert an upward electrostatic force on the flexures of the device as well as the downward force on the mirror surface. The separation distance between the flexures and electrode is only 0.5 μm which significantly increases the magnitude of the electrostatic force between them. When the effects of a continuous force along a beam is analyzed, it is easy to see that the length of the flexures will reach some critical value in which the area is sufficient to pull the flexures upward rather than the mirror downward. For flexures shorter than this critical length, the behavior of the device will diverge from the ideal model for small deflections due to the adverse effect of this counteracting force. As the device reaches greater deflections, however, the distance between the flexures and the electrode increases whereas the distance between the electrode and mirror surface decreases. Therefore, the device more closely conforms to the ideal model at the upper end of the deflection versus applied potential curve.

Another characteristic which should be considered in device modeling is the use of upper and lower address plates having different areas. Most models of the Flexure-Beam device ignore fringing effects between the two plates provided their area is sufficient to do so. However, should one plate be considerably larger than the other, significant additional forces will act between the plates along the electric field lines emanating from the edges of the smaller address plate. This effect can easily be observed in devices in which the mirror surface is suspended over an address electrode that is reduced in size in order to allow for additional address wiring beneath the device.

The ideal Flexure-Beam model determines the address potential, V, that is required to actuate a device of specific dimensions to a desired deflection, d, such that:

$$V = (z_0 - d)\sqrt{\frac{2kd}{\varepsilon_0 A}} \qquad k \approx N\left[\frac{Ewt^3}{L^3}\right] \qquad (1)$$

where z_o, k, ε_o, and A are the resting separation distance, spring constant, permittivity of free space, and electrode area, respectively. The spring constant is also shown in Equation (1) in which L, w, t, and E are the length, width, thickness, and modulus of elasticity of N identical flexures, respectively [3]. (This simplified spring constant does not include stress terms which would typically affect micromirror device operation due to the ultra-low-stress polysilicon used in the SUMMiT fabrication process.) ~~awkward sentence~~

Using numerous devices, both the advanced and ideal models for the Flexure-Beam micromirror have been used to extract the material properties for the structural layers forming the flexures. In order to do so, however, the actual thickness and width of the flexures should be precisely measured using high-magnification SEM micrographs or similar techniques. The spring constant in Equation (1) depends heavily on the dimensions of the flexures which may not be the exact design dimensions or target thickness of the layer due to overetching or improper mask alignment. A value for the effective modulus of elasticity is obtained by simply fitting the model to the data using the spring constant. To extract highly accurate values, however, devices should be used that do not have characteristics such as raised address electrodes, wrapped flexures, overhanging mirror surfaces, or other features that would normally be neglected by the ideal model.

CHARACTERIZATION

The interferometric experimental setup used to characterize the micromirror devices is shown in Figure 5 which illustrates that the device under test is placed inside a test chamber positioned upon a precision tip/tilt translation stage. This test chamber is first evacuated, flooded with dry nitrogen, and then evacuated again to a constant pressure of 20 mTorr in order to remove damping effects observed in open air. This chamber can also be thermally controlled in order to study behavior variations as a function of temperature [4]. The chamber has four internal micromanipulator probes that are used to establish electrical contacts with the device. When repressurizing the test chamber, extreme care, patience, and an accurate pressure gauge are helpful to avoid launching the test chip into another time zone.
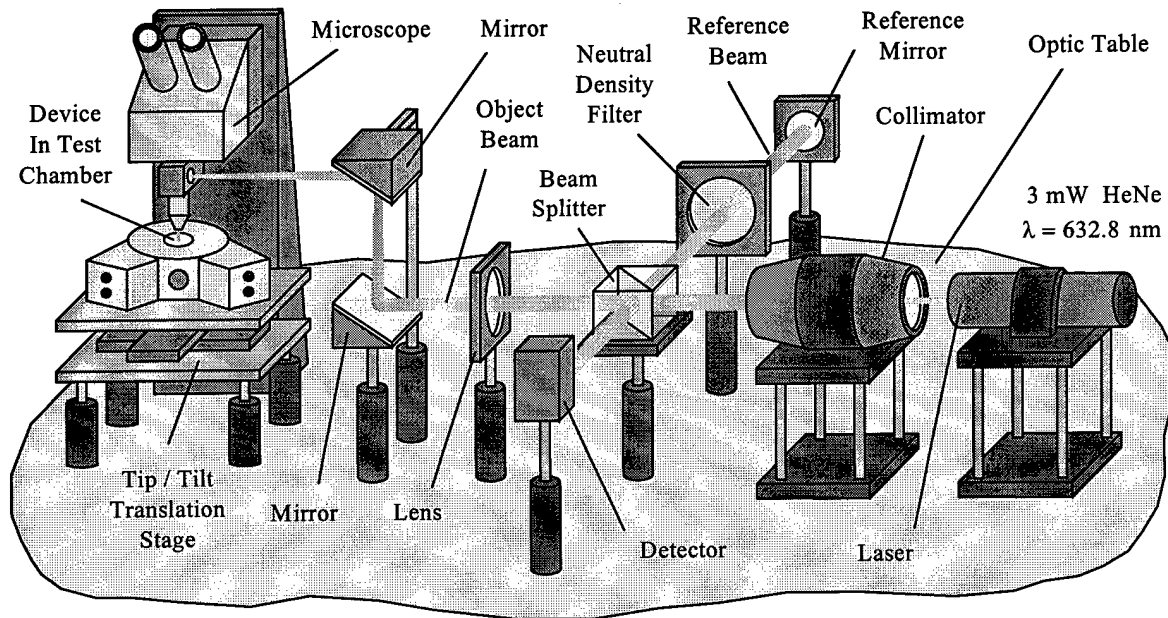

Figure 5. Schematic representation of the laser interferometer experimental setup [4].

The device is actuated with a sinusoidal potential which moves the reflective surface and controllably lengthens the optical path of the object beam. When the object and reference beams are joined at the beam splitter, the classic interference pattern is observed by the photodetector which produces a current relative to the optical intensity. A high-gain precision transimpedance amplifier is used to generate an output signal which can be compared to the input drive signal to form a characteristic deflection versus applied potential curve [5]. The object beam can be focused onto the mirror surface of the device under test with a spot size of only 4 μm or less. Therefore, by using the electronically-controlled translation stage, a very precise deflection mapping of the mirror surface can be obtained by characterizing the device at numerous points along the surface using the same address signal.

For most devices, the address signal can be applied using a standard signal generator. However, devices requiring significantly higher address potentials (greater than 25 volts) were tested using a signal processing step-up transformer to amplify the input signal in series with a high-voltage power supply for a DC offset. This setup provides a reliable sinusoidal address signal ranging from zero to approximately 150 volts maximum provided the signal frequency is above some critical value in which the transformer displays a significant hysteresis.

The primary Flexure-Beam device studied in this paper was selected because of its geometry and subsequently low address potential. This device, shown in Figure 6, has an upper address plate and four flexures of stacked Poly-1 and Poly-2 construction. Stacked devices are realized by masking specific features in Poly-2 that is deposited directly on top of the previous unmasked Poly-1 layer. The masked etch removes all the excess Poly-1 that is not covered by the Poly-2 mask. These linear flexures are more easily modeled using standard beam theory whereas flexures which curve around the device require a more complicated model [4]. The 200 x 200 μm planarized mirror surface, which provides an unprecedented 98.4% optical efficiency, is attached to the upper plate via four support posts. Because the edges of the device extend well beyond the position of the supporting flexures, any tilting during actuation can be more easily detected and quantified.
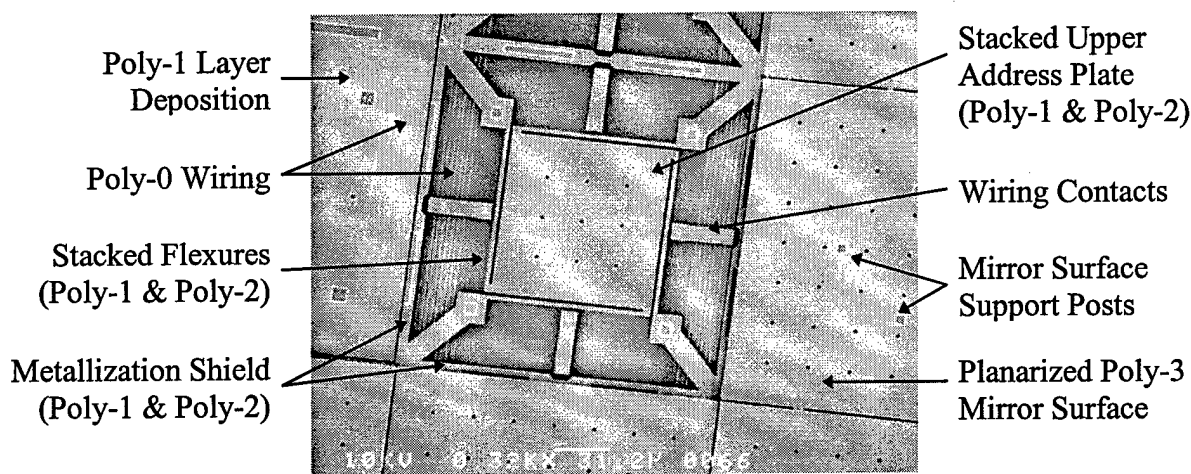

Figure 6. Layer depiction of the primary Flexure-Beam Micromirror Device under test.

Furthermore, the support posts which attach the mirror surface to the upper address plate make the device resistant to deformations at its center which are often observed in devices of this size during actuation. In order to verify this property, each device will be characterized at five points, the center and four corners of the mirror surface.

The devices were tested at a drive frequency of 2.8 kHz in order to demonstrate the effects of squeeze-film damping which are easily observed when operating such a large device in air. These effects drop off with the frequency until a more ideal behavior is observed at near static actuation. At higher frequencies, however, the test setup demonstrates a capacitive hysteresis in the photodetector and transimpedance amplifier. These effects diminish the relative maximum and minimum peaks in the output signal associated with the in-phase and out-of-phase alignment, respectively. As a result, the behavior curves begin to show two distinct regions where the empirical data diverges from the model.

The effective modulus of elasticity was extracted from Equation (1) using the fitted spring constant of 14.72 N/m for this Flexure-Beam device. Given the design dimensions, the modulus was found to be 139 GPa which is significantly lower than the known value of approximately 160 GPa for polycrystalline silicon. This is partially due to the fringing forces between the address electrode and the mirror surface, wiring, and elevated wiring contacts were neglected. By ignoring the added electrostatic force supplied along these electric field lines, it was assumed the flexures were comparatively more compliant which represents a lower spring constant. Additionally, the design dimensions were used rather than obtaining exact measurements of the flexures. Due to overetching and calculating the layer thickness, the dimensions of the flexures may vary significantly from the design values and target

thickness of the structural layer. These neglected features equate to a moderate error in determining the modulus of elasticity from this spring constant. If the material properties are to be precisely measured, a Flexure-Beam device should be employed which does not possess these design features and its actual flexure dimensions should be used.

The experimental data for the Flexure-Beam device under test consists of five traces on one device operated in a vacuum. The traces were located at the center and four corners of the device to determine any deformations or tilting of the mirror surface. These data curves are shown in Figure 7 along with the ideal model given in Equation (1) which was fit to this empirical data. The center of the same device was also characterized in air to demonstrate squeeze-film damping effects. Of particular interest are two traces obtained from the opposite corners of a second device found in the same array. These traces illustrate that the device tilts during actuation most likely due to a damaged flexure or trapped particulate matter.
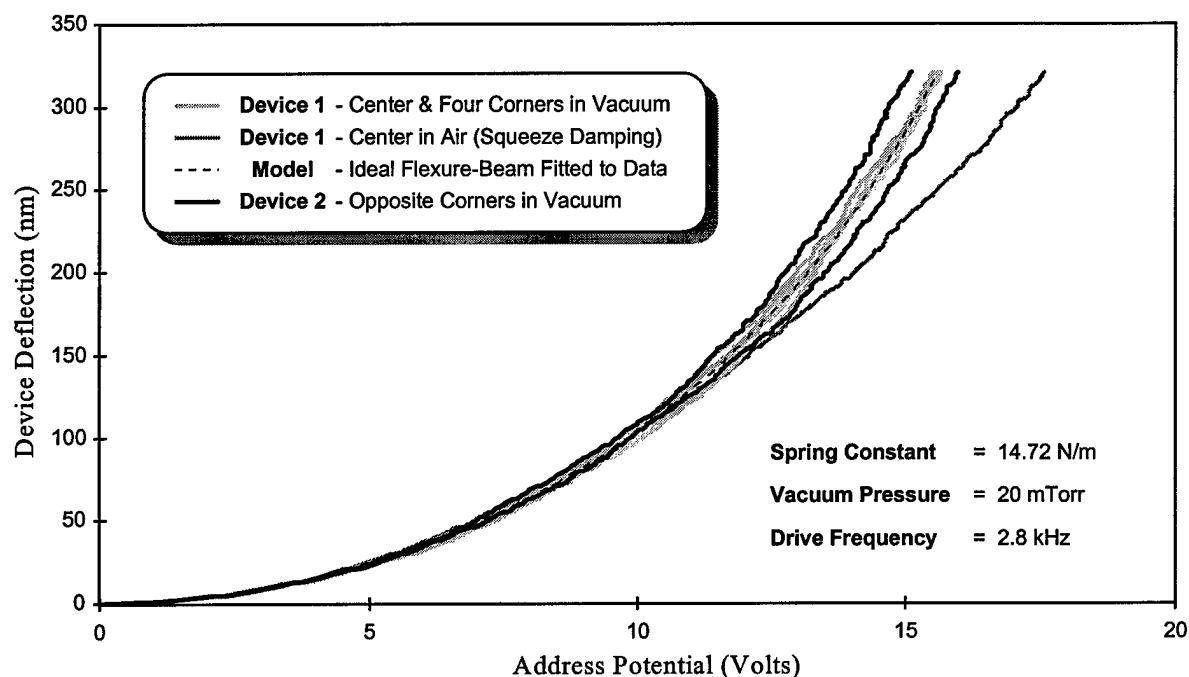

Figure 7. Plot of characteristic behavior curves for the Flexure-Beam Micromirror Device.

The primary device, however, demonstrates a maximum variance of only 9 nm between all five points. Given a system error of only 2-4 nm for each trace, this device appears to operate well within an expected region described by the ideal Flexure-Beam model.

Due to the exponential nature of the device behavior, the squeeze-film damping effects are not observed at the lower end of the curve because of the actual velocity of the mirror surface. When driven by a sinusoidal address potential, the device must travel through the majority of its deflection distance during only the upper portion of the drive signal. This increased velocity of the mirror surface intensifies the squeeze-film effects. Therefore, the device appears to behave in air as it would in a vacuum until the upper end of the curve where it begins to diverge from this behavior as given by the ideal model.

To determine a damping coefficient versus micromirror dimensions, a wide range of test devices can be similarly characterized in air using an advanced model that includes damping effects. This model can be derived from the equations of a damped harmonic oscillator which is driven by a sinusoidal force [6]. Such test devices, already designed for future SUMMiT fabrication, have identical structures beneath mirror surfaces of varying area.

Also characterized were four designs of Axial-Rotation devices, such as the one shown in Figure 2(b), in which the mirror surface deflects toward any angle about the normal to the substrate depending on the relative address potentials applied to four address electrodes per device. Three of the designs possessed short flexures intended for bending which behaved as expected, but required significant address potentials (~120 volts) to fully deflect toward one side. The fourth design, however, consisted of dual torsion flexures in which two opposite corners were anchored to the substrate and the other two supported the mirror surface. Although this device actuated at significantly less potential (~75 volts), it was observed that the mirror surface tilted dramatically during actuation. The device tilted away from the support posts indicating that the supporting flexure was much more resistant to bending than the mirror flexure. This device shows promise for future use provided the torsion properties of the two flexures can be sufficiently modeled to balance their behavior.

CONCLUSIONS

This research has clearly shown the advantages of the SUMMiT process for the fabrication of highly-advanced micromirror devices demonstrating unprecedented optical efficiencies. The advanced features of this process allows for the design of more complex micromirrors and larger arrays of individually addressable devices with near-ideal optical flatness and mechanical uniformity across the array. The variety of structural layers permits the address potentials of these devices to be easily tailored to suit the needs of the application.

ACKNOWLEDGMENTS

REFERENCES

[1]   E. J. Garcia and J. J. Sniegowski, "*Surface Micromachined Microengine*", Sensors and Actuators A 48 (1995) 203-214.

[2]   D. Koester, R. Mahedevan, and K. Marcus, *Multi-User MEMS Processes (MUMPS) Introduction and Design Rules*, revision 3, Oct 1994, MCNC MEMS Technology Applications Center, 3021 Cornwallis Road, RTP, NC, 27709.

[3]   M. A. Michalicek, V. M. Bright, and J. H. Comtois, "*Design, fabrication, modeling, and testing of a surface-micromachined micromirror device*," Proc. ASME, DSC vol. 57-2, pp 981-988, 1995.

[4]   M. A. Michalicek, D. E. Sene, and V. M. Bright, "*Advanced modeling of micromirror devices*," Proc. Integrated Micro/Nanotechnology for Space Applications, NASA and Aerospace Press, pp. 214-229, 30 October 1995.

[5]   T. A. Rhoadarmer, V. M. Bright, B. M. Welsh, S. C. Gustafson, and T. H. Lin, "*Interferometric characterization of the flexure beam micromirror device*," Proc. SPIE, Vol. 2291, 1994, pp. 13-23.

[6]   J. B. Marion and S. T. Thornton. Classical Dynamics of Particles & Systems. 3 ed. Harcourt Brace Jovanovich, San Diego, 1988.

Report Number (14) _SAND--97-2532C_
CONF-971088--

Publ. Date (11) _199710_
Sponsor Code (18) _DOE/MA, XF_
UC Category (19) _UC-900, DOE/ER_

DOE